PNAS
www.pnas.org

Supplementary Information for

Multiresponsive polymeric microstructures with encoded predetermined and self-regulated deformability

Yuxing Yao[a], James T. Waters[b], Anna V. Shneidman[c], Jiaxi Cui[c], Xiaoguang Wang[c], Nikolaj K. Mandsberg[c,d], Shucong Li[a], Anna C. Balazs[b], Joanna Aizenberg[a,c,e,1]

[a]Department of Chemistry and Chemical Biology, Harvard University, Cambridge, MA 02138, USA [b]Chemical Engineering Department, University of Pittsburgh, Pittsburgh, PA 15261, USA [c]John A. Paulson School of Engineering and Applied Sciences, Harvard University, Cambridge, MA 02138, USA [d]Department of Micro- and Nanotechnology, Technical University of Denmark, 2800 Kongens Lyngby, Denmark [e]Wyss Institute for Biologically Inspired Engineering, Harvard University, Cambridge, MA 02138, USA
[1]To whom correspondence may be addressed. Email: jaiz@seas.harvard.edu

www.pnas.org/cgi/doi/10.1073/pnas.1811823115

This PDF file includes:

Other supplementary materials for this manuscript include the following:

1. Materials

2,5-Dihydroxybenzoic acid, benzyl bromide, 4-butyloxybenzoic acid, 4-hydroxybutyl acrylate, 4-hydroxybenzophenone, Rhodamine B dye, anhydrous dichloromethane and deuterated chloroform were obtained from Sigma Aldrich. 4,4'-Bis(6-acryloyloxyhexyloxy) azobenzene was purchased from Synthon. Bis(2,4,6-trimethylbenzoyl)-phenylphosphineoxide was obtained from Ciba Specialty Chemical Inc. All of the above was used without further purification. 1,6-Hexanediol diacrylate was obtained from Sigma Aldrich, and the inhibitor was removed prior to use. Si wafers were purchased from Nova Electronic Materials. Photoresist SPR220-4.5 was purchased from Microchem. Sylgard 184 silicone kit was purchased from Ellsworth Adhesive Systems. Cover glass (22 mm in diameter, 0.21 mm in thickness) was obtained from VWR. The NdFeB-based magnet with different shapes and dimensions were purchased from K&J Magnetics, Inc.

2. Synthesis and characterization of the liquid crystalline elastomer (LCE)

2.1. Synthesis of the LC monomer

The LC monomer 4″-acryloyloxybutyl 2,5-di(4′-butyloxybenzoyloxy) benzoate was synthesized following the route described by Thomsen et al. (1). The chemical structure of the monomer was confirmed by ^{1}H NMR using Varian I500C 500 MHz spectrometer, as evidenced by the ^{1}H spectrum of the LC monomer shown in Fig. S1.

2.2. Phase behavior of the LC monomer mixture and the polymeric network

The phase behavior of the monomer mixture was studied with differential scanning calorimetry (DSC) and polarized optical microscopy (POM). DSC measurements were conducted using Thermal Analysis DSC Q200 with a rate of 10^{o}C/min. POM imaging was carried out under Zeiss Axio Imager 2. The thermal-responsive reactive mixture showed a nematic phase in the temperature range of 52-86^{o}C, as shown in Fig. S2a,b. After polymerization, the LCE showed a glass transition temperature (T_g) at 40^{o}C and a nematic-isotropic (N-I) phase transition at about 125^{o}C (Fig. S2c,d).

3. Finite element simulations of LCE microplate deformations

The elasticity of the polymeric material is described by the Gent model (2,3), a modification of Neo-Hookean elasticity, chosen to correct for the finite extensibility of polymer chains. The free energy of the elasticity is expressed as:

$$F_{el} = -\frac{\mu(I_m - 3)}{2}\log\left(\frac{I_m - I_1}{I_m - 3}\right) + \frac{K}{2}\log^2 J + UQ_{ab}\bar{\varepsilon}_{ab} \quad (0.1)$$

The first term describes the resistance of the material to shear deformations, where μ is the shear modulus, here assumed to be 570 kPa (4,5), and I_1 is the first invariant of the right Cauchy-Green deformation tensor $\boldsymbol{\varepsilon}$. The constant I_m defines the limit of uniaxial extensibility, here assumed to be thirty times the initial extension. Far from this limit, the dependence of free energy on extension is approximately linear, corresponding to the Neo-Hookean model; as the material approaches the limit of extensibility, this will

rapidly diverge. The second term corresponds to the bulk modulus, the resistance of the material to changes in volume, where K is the bulk modulus, equal to 28 MPa (4), and J is the volume of the element. J is equivalent to the square root of the third invariant of the tensor $\boldsymbol{\varepsilon}$. The third term represents the coupling of the material strain to the nematic ordering. The tensor $\bar{\boldsymbol{\varepsilon}}$ represents the right Cauchy-Green tensor $\boldsymbol{\varepsilon}$ normalized by a power of the local differential volume, $J^{2/3}$. The traceless tensor Q_{ab} is derived from the nematic director $\mathbf{n}$ multiplied by the change in order parameter ΔS between the ordered, nematic state in which the elastomer was cross-linked and the present isotropic state.

$$Q_{ab} = \Delta S\left(n_a n_b - \frac{1}{3}\delta_{ab} \right) \qquad (0.2)$$

Where the n_a are components of the nematic director and δ_{ab} is the Kronecker delta. U is a constant describing the coupling of strain in the elastomer to changes in nematic order. The ratio of the product $U\Delta S$ to the shear modulus μ was obtained from experimental measurement of the dimensional changes of a free microplate as it underwent a transition from a nematic to an isotropic state, shown in Fig. S6. A value of 80 kPa was used for $U\Delta S$ in the simulations.

Our implementation makes use of a hexahedral finite element (Fig. S3), assumed to be initially cubic. Each element has initial dimensions of $10\mu m \times 10\mu m \times 10\mu m$, so the $250\mu m \times 50\mu m \times 200\mu m$ plate is represented by 2500 finite elements with 3276 vertices. The mass of each element is divided evenly between its eight corners. As a result, internal nodes of the finite element mesh will have a mass of $10^{-9} g$, equal to that of a single cubic element. Nodes on faces, edges, and corners of the plate will have smaller masses of $5.0\times10^{-10} g$, $2.5\times10^{-10} g$, and $1.25\times10^{-10} g$, respectively. The material frame coordinates α, β, γ range from -1 to +1 within each volume element, with the nodes defining the vertices numbered as shown in Fig. S3. Any point inside the element can be expressed as a linear combination of the node coordinates, as shown in equation (0.3). The coefficients on each $\mathbf{r}_i$ are the shape functions, used to interpolate solutions between the discrete nodal coordinates.

$$\mathbf{r} = \frac{1}{8}\begin{pmatrix} +(1-\alpha)(1-\beta)(1-\gamma)\mathbf{r}_0 & +(1+\alpha)(1-\beta)(1-\gamma)\mathbf{r}_1 \\ +(1-\alpha)(1+\beta)(1-\gamma)\mathbf{r}_2 & +(1+\alpha)(1+\beta)(1-\gamma)\mathbf{r}_3 \\ +(1-\alpha)(1-\beta)(1+\gamma)\mathbf{r}_4 & +(1+\alpha)(1-\beta)(1+\gamma)\mathbf{r}_5 \\ +(1-\alpha)(1+\beta)(1+\gamma)\mathbf{r}_6 & +(1+\alpha)(1+\beta)(1+\gamma)\mathbf{r}_7 \end{pmatrix} \qquad (0.3)$$

The deformation gradient tensor, λ, can then be obtained from the relationship between the material-frame coordinates and those in the lab-frame. Generally, this is expressed as

$$\boldsymbol{\lambda} = \begin{pmatrix} \frac{\partial x}{\partial \alpha} & \frac{\partial x}{\partial \beta} & \frac{\partial x}{\partial \gamma} \\ \frac{\partial y}{\partial \alpha} & \frac{\partial y}{\partial \beta} & \frac{\partial y}{\partial \gamma} \\ \frac{\partial z}{\partial \alpha} & \frac{\partial z}{\partial \beta} & \frac{\partial z}{\partial \gamma} \end{pmatrix} \quad (0.4)$$

We can simplify this in our particular case by introducing several auxiliary vectors, composed of combinations of the nodal coordinates defining the element.

$$\begin{aligned} \mathbf{r}_{\alpha} &= (-\mathbf{r}_0 + \mathbf{r}_1 - \mathbf{r}_2 + \mathbf{r}_3 - \mathbf{r}_4 + \mathbf{r}_5 - \mathbf{r}_6 + \mathbf{r}_7)/8 \\ \mathbf{r}_{\beta} &= (-\mathbf{r}_0 - \mathbf{r}_1 + \mathbf{r}_2 + \mathbf{r}_3 - \mathbf{r}_4 - \mathbf{r}_5 + \mathbf{r}_6 + \mathbf{r}_7)/8 \\ \mathbf{r}_{\gamma} &= (-\mathbf{r}_0 - \mathbf{r}_1 - \mathbf{r}_2 - \mathbf{r}_3 + \mathbf{r}_4 + \mathbf{r}_5 + \mathbf{r}_6 + \mathbf{r}_7)/8 \\ \mathbf{r}_{\alpha\beta} &= (+\mathbf{r}_0 - \mathbf{r}_1 - \mathbf{r}_2 + \mathbf{r}_3 + \mathbf{r}_4 - \mathbf{r}_5 - \mathbf{r}_6 + \mathbf{r}_7)/8 \\ \mathbf{r}_{\alpha\gamma} &= (+\mathbf{r}_0 - \mathbf{r}_1 + \mathbf{r}_2 - \mathbf{r}_3 - \mathbf{r}_4 + \mathbf{r}_5 - \mathbf{r}_6 + \mathbf{r}_7)/8 \\ \mathbf{r}_{\beta\gamma} &= (+\mathbf{r}_0 + \mathbf{r}_1 - \mathbf{r}_2 - \mathbf{r}_3 - \mathbf{r}_4 - \mathbf{r}_5 + \mathbf{r}_6 + \mathbf{r}_7)/8 \\ \mathbf{r}_{\alpha\beta\gamma} &= (-\mathbf{r}_0 + \mathbf{r}_1 + \mathbf{r}_2 - \mathbf{r}_3 + \mathbf{r}_4 - \mathbf{r}_5 - \mathbf{r}_6 + \mathbf{r}_7)/8 \end{aligned} \quad (0.5)$$

This allows us to write the derivatives of the lab-frame position with respect to the element coordinates as

$$\begin{aligned} \partial\mathbf{r}/\partial\alpha &= \mathbf{r}_{\alpha} + \beta\mathbf{r}_{\alpha\beta} + \gamma\mathbf{r}_{\alpha\gamma} + \beta\gamma\mathbf{r}_{\alpha\beta\gamma} \\ \partial\mathbf{r}/\partial\beta &= \mathbf{r}_{\beta} + \alpha\mathbf{r}_{\alpha\beta} + \gamma\mathbf{r}_{\beta\gamma} + \alpha\gamma\mathbf{r}_{\alpha\beta\gamma} \\ \partial\mathbf{r}/\partial\gamma &= \mathbf{r}_{\gamma} + \alpha\mathbf{r}_{\alpha\gamma} + \beta\mathbf{r}_{\beta\gamma} + \alpha\beta\mathbf{r}_{\alpha\beta\gamma} \end{aligned} \quad (0.6)$$

Components of these vectors fill out the deformation gradient tensor.

$$\boldsymbol{\lambda} = \begin{pmatrix} x_{\alpha} + \beta x_{\alpha\beta} + \gamma x_{\alpha\gamma} + \beta\gamma x_{\alpha\beta\gamma} & x_{\beta} + \alpha x_{\alpha\beta} - \gamma x_{\beta\gamma} + \alpha\gamma x_{\alpha\beta\gamma} & x_{\gamma} + \alpha x_{\alpha\gamma} + \beta x_{\beta\gamma} + \alpha\beta x_{\alpha\beta\gamma} \\ y_{\alpha} + \beta y_{\alpha\beta} + \gamma y_{\alpha\gamma} + \beta\gamma y_{\alpha\beta\gamma} & y_{\beta} + \alpha y_{\alpha\beta} - \gamma y_{\beta\gamma} + \alpha\gamma y_{\alpha\beta\gamma} & y_{\gamma} + \alpha y_{\alpha\gamma} + \beta y_{\beta\gamma} + \alpha\beta y_{\alpha\beta\gamma} \\ z_{\alpha} + \beta z_{\alpha\beta} + \gamma z_{\alpha\gamma} + \beta\gamma z_{\alpha\beta\gamma} & z_{\beta} + \alpha z_{\alpha\beta} - \gamma z_{\beta\gamma} + \alpha\gamma z_{\alpha\beta\gamma} & z_{\gamma} + \alpha z_{\alpha\gamma} + \beta z_{\beta\gamma} + \alpha\beta z_{\alpha\beta\gamma} \end{pmatrix} \quad (0.7)$$

The right Cauchy-Green tensor $\boldsymbol{\varepsilon}$ is then found from the product $\boldsymbol{\lambda}^T\boldsymbol{\lambda}$, contracting the deformation gradient tensor with itself over the lab-frame coordinates. This is then used for computing the free energy cost of deformations. Integrating the transcendental functions of the tensor invariants in Equation (0.1) over the element is intractable for most expressions of energy; instead we turn to an eight-point Gaussian integration evaluated at the points $(\alpha,\beta,\gamma) = \left(\pm\frac{1}{\sqrt{3}}, \pm\frac{1}{\sqrt{3}}, \pm\frac{1}{\sqrt{3}}\right)$. The first invariant, the trace of the tensor $\boldsymbol{\varepsilon}$, is expressed at each of these points as

$$I_1 = (\partial\mathbf{r}/\partial\alpha)^2 + (\partial\mathbf{r}/\partial\beta)^2 + (\partial\mathbf{r}/\partial\gamma)^2 \quad (0.8)$$

The determinant of the deformation gradient tensor can similarly be found:

$$J = \partial\mathbf{r}/\partial\alpha \bullet (\partial\mathbf{r}/\partial\beta \times \partial\mathbf{r}/\partial\gamma) \quad (0.9)$$

Differentiating the free energy with respect to the nodal coordinates allows us to determine the force on each point i, and to update accelerations at each timestep:

$$\mathbf{f_i} = -\frac{\mu}{2}\frac{I_m - 3}{I_m - I_1}\nabla_i I_1 - K\log J\frac{\nabla_i J}{J} + U\Delta S\left(\frac{\nabla_i n_a n_b \varepsilon_{ab}}{J^{2/3}} - \frac{\nabla_i I_1}{3J^{2/3}} - \frac{2(n_a n_b \varepsilon_{ab} - I_1/3)\nabla_i J}{3J^{5/3}}\right)$$

(0.10)

For each of the eight nodes comprising the element, we can express the derivatives of the invariants required in the force expression. For the first invariant, I_1 , we have the following relations:

$$\begin{aligned}
4\nabla_0 I_1 &= -(1-\beta)(1-\gamma)\partial\mathbf{r}/\partial\alpha \quad -(1-\alpha)(1-\gamma)\partial\mathbf{r}/\partial\beta \quad -(1-\alpha)(1-\beta)\partial\mathbf{r}/\partial\gamma \\
4\nabla_1 I_1 &= +(1-\beta)(1-\gamma)\partial\mathbf{r}/\partial\alpha \quad -(1+\alpha)(1-\gamma)\partial\mathbf{r}/\partial\beta \quad -(1+\alpha)(1-\beta)\partial\mathbf{r}/\partial\gamma \\
4\nabla_2 I_1 &= -(1+\beta)(1-\gamma)\partial\mathbf{r}/\partial\alpha \quad +(1-\alpha)(1-\gamma)\partial\mathbf{r}/\partial\beta \quad -(1-\alpha)(1+\beta)\partial\mathbf{r}/\partial\gamma \\
4\nabla_3 I_1 &= +(1+\beta)(1-\gamma)\partial\mathbf{r}/\partial\alpha \quad +(1+\alpha)(1-\gamma)\partial\mathbf{r}/\partial\beta \quad -(1+\alpha)(1+\beta)\partial\mathbf{r}/\partial\gamma \\
4\nabla_4 I_1 &= -(1-\beta)(1+\gamma)\partial\mathbf{r}/\partial\alpha \quad -(1-\alpha)(1+\gamma)\partial\mathbf{r}/\partial\beta \quad +(1-\alpha)(1-\beta)\partial\mathbf{r}/\partial\gamma \\
4\nabla_5 I_1 &= +(1-\beta)(1+\gamma)\partial\mathbf{r}/\partial\alpha \quad -(1+\alpha)(1+\gamma)\partial\mathbf{r}/\partial\beta \quad +(1+\alpha)(1-\beta)\partial\mathbf{r}/\partial\gamma \\
4\nabla_6 I_1 &= -(1+\beta)(1+\gamma)\partial\mathbf{r}/\partial\alpha \quad +(1-\alpha)(1+\gamma)\partial\mathbf{r}/\partial\beta \quad +(1-\alpha)(1+\beta)\partial\mathbf{r}/\partial\gamma \\
4\nabla_7 I_1 &= +(1+\beta)(1+\gamma)\partial\mathbf{r}/\partial\alpha \quad +(1+\alpha)(1+\gamma)\partial\mathbf{r}/\partial\beta \quad +(1+\alpha)(1+\beta)\partial\mathbf{r}/\partial\gamma
\end{aligned}$$

(0.11)

For the volume element J , we find

$$\begin{aligned}
8\nabla_0 J &= -(1-\beta)(1-\gamma)\partial\mathbf{r}/\partial\beta\times\partial\mathbf{r}/\partial\gamma \quad -(1-\alpha)(1-\gamma)\partial\mathbf{r}/\partial\gamma\times\partial\mathbf{r}/\partial\alpha \quad -(1-\alpha)(1-\beta)\partial\mathbf{r}/\partial\alpha\times\partial\mathbf{r}/\partial\beta \\
8\nabla_1 J &= +(1-\beta)(1-\gamma)\partial\mathbf{r}/\partial\beta\times\partial\mathbf{r}/\partial\gamma \quad -(1+\alpha)(1-\gamma)\partial\mathbf{r}/\partial\gamma\times\partial\mathbf{r}/\partial\alpha \quad -(1+\alpha)(1-\beta)\partial\mathbf{r}/\partial\alpha\times\partial\mathbf{r}/\partial\beta \\
8\nabla_2 J &= -(1+\beta)(1-\gamma)\partial\mathbf{r}/\partial\beta\times\partial\mathbf{r}/\partial\gamma \quad +(1-\alpha)(1-\gamma)\partial\mathbf{r}/\partial\gamma\times\partial\mathbf{r}/\partial\alpha \quad -(1-\alpha)(1+\beta)\partial\mathbf{r}/\partial\alpha\times\partial\mathbf{r}/\partial\beta \\
8\nabla_3 J &= +(1+\beta)(1-\gamma)\partial\mathbf{r}/\partial\beta\times\partial\mathbf{r}/\partial\gamma \quad +(1+\alpha)(1-\gamma)\partial\mathbf{r}/\partial\gamma\times\partial\mathbf{r}/\partial\alpha \quad -(1+\alpha)(1+\beta)\partial\mathbf{r}/\partial\alpha\times\partial\mathbf{r}/\partial\beta \\
8\nabla_4 J &= -(1-\beta)(1+\gamma)\partial\mathbf{r}/\partial\beta\times\partial\mathbf{r}/\partial\gamma \quad -(1-\alpha)(1+\gamma)\partial\mathbf{r}/\partial\gamma\times\partial\mathbf{r}/\partial\alpha \quad +(1-\alpha)(1-\beta)\partial\mathbf{r}/\partial\alpha\times\partial\mathbf{r}/\partial\beta \\
8\nabla_5 J &= +(1-\beta)(1+\gamma)\partial\mathbf{r}/\partial\beta\times\partial\mathbf{r}/\partial\gamma \quad -(1+\alpha)(1+\gamma)\partial\mathbf{r}/\partial\gamma\times\partial\mathbf{r}/\partial\alpha \quad +(1+\alpha)(1-\beta)\partial\mathbf{r}/\partial\alpha\times\partial\mathbf{r}/\partial\beta \\
8\nabla_6 J &= -(1+\beta)(1+\gamma)\partial\mathbf{r}/\partial\beta\times\partial\mathbf{r}/\partial\gamma \quad +(1-\alpha)(1+\gamma)\partial\mathbf{r}/\partial\gamma\times\partial\mathbf{r}/\partial\alpha \quad +(1-\alpha)(1+\beta)\partial\mathbf{r}/\partial\alpha\times\partial\mathbf{r}/\partial\beta \\
8\nabla_7 J &= +(1+\beta)(1+\gamma)\partial\mathbf{r}/\partial\beta\times\partial\mathbf{r}/\partial\gamma \quad +(1+\alpha)(1+\gamma)\partial\mathbf{r}/\partial\gamma\times\partial\mathbf{r}/\partial\alpha \quad +(1+\alpha)(1+\beta)\partial\mathbf{r}/\partial\alpha\times\partial\mathbf{r}/\partial\beta
\end{aligned}$$

(0.12)

Finally, we obtain one additional set of vectors necessary for the derivative of the nematic energy:

$$\begin{aligned}
4\nabla_0 n_b n_a \varepsilon_{ab} &= (n_x\partial\mathbf{r}/\partial\alpha + n_y\partial\mathbf{r}/\partial\beta + n_z\partial\mathbf{r}/\partial\gamma)(-n_x(1-\beta)(1-\gamma) - n_y(1-\alpha)(1-\gamma) - n_z(1-\alpha)(1-\beta)) \\
4\nabla_1 n_b n_a \varepsilon_{ab} &= (n_x\partial\mathbf{r}/\partial\alpha + n_y\partial\mathbf{r}/\partial\beta + n_z\partial\mathbf{r}/\partial\gamma)(+n_x(1-\beta)(1-\gamma) - n_y(1+\alpha)(1-\gamma) - n_z(1+\alpha)(1-\beta)) \\
4\nabla_2 n_b n_a \varepsilon_{ab} &= (n_x\partial\mathbf{r}/\partial\alpha + n_y\partial\mathbf{r}/\partial\beta + n_z\partial\mathbf{r}/\partial\gamma)(-n_x(1+\beta)(1-\gamma) + n_y(1-\alpha)(1-\gamma) - n_z(1-\alpha)(1+\beta)) \\
4\nabla_3 n_b n_a \varepsilon_{ab} &= (n_x\partial\mathbf{r}/\partial\alpha + n_y\partial\mathbf{r}/\partial\beta + n_z\partial\mathbf{r}/\partial\gamma)(+n_x(1+\beta)(1-\gamma) + n_y(1+\alpha)(1-\gamma) - n_z(1+\alpha)(1+\beta)) \\
4\nabla_4 n_b n_a \varepsilon_{ab} &= (n_x\partial\mathbf{r}/\partial\alpha + n_y\partial\mathbf{r}/\partial\beta + n_z\partial\mathbf{r}/\partial\gamma)(-n_x(1-\beta)(1+\gamma) - n_y(1-\alpha)(1+\gamma) + n_z(1-\alpha)(1-\beta)) \\
4\nabla_5 n_b n_a \varepsilon_{ab} &= (n_x\partial\mathbf{r}/\partial\alpha + n_y\partial\mathbf{r}/\partial\beta + n_z\partial\mathbf{r}/\partial\gamma)(+n_x(1-\beta)(1+\gamma) - n_y(1+\alpha)(1+\gamma) + n_z(1+\alpha)(1-\beta)) \\
4\nabla_6 n_b n_a \varepsilon_{ab} &= (n_x\partial\mathbf{r}/\partial\alpha + n_y\partial\mathbf{r}/\partial\beta + n_z\partial\mathbf{r}/\partial\gamma)(-n_x(1+\beta)(1+\gamma) + n_y(1-\alpha)(1+\gamma) + n_z(1-\alpha)(1+\beta)) \\
4\nabla_7 n_b n_a \varepsilon_{ab} &= (n_x\partial\mathbf{r}/\partial\alpha + n_y\partial\mathbf{r}/\partial\beta + n_z\partial\mathbf{r}/\partial\gamma)(+n_x(1+\beta)(1+\gamma) + n_y(1+\alpha)(1+\gamma) + n_z(1+\alpha)(1+\beta))
\end{aligned}$$

(0.13)

The above expressions are used to evaluate the force on each of the eight corners of an element, at each of the eight Gaussian integration points. After obtaining the force, the system is advanced in time using a leapfrog integration method to update the position $\mathbf{r}_i$

and velocity $\mathbf{v}_i$ of each node using the acceleration $\mathbf{a}_i$ found from the force in equation (0.10).

$$\mathbf{r}_{i+1} = \mathbf{r}_i + \mathbf{v}_i \Delta t + \frac{1}{2}\mathbf{a}_i \Delta t^2$$

$$\mathbf{v}_{i+1} = (1-\eta)\mathbf{v}_i + \frac{1}{2}(\mathbf{a}_i + \mathbf{a}_{i+1})\Delta t \qquad (0.14)$$

A timestep, Δt, of $10^{-7} s$, for 10^6 timesteps, was chosen to allow the system to achieve a stable final state. The factor η represents the simplest means of implementing damping to allow the system to halt in equilibrium rather than oscillating indefinitely, with a resistance linearly proportional to velocity as is encountered in viscous drag. Simulations were run with a value of $\eta = 0.1$, corresponding to a damping coefficient of 10^{-5} kg/s; the value of this parameter will not affect the final shape of the LCE structure.

4. Fabrication and characterization of thermal-responsive LCE microstructures with variable deformation behaviors

4.1. Fabrication of microstructured PDMS molds

Si microstructures were made by photolithography followed by reactive ion etching (RIE). Photoresist (SPR220-4.5) patterning was performed by the UV exposure under a Heidelberg MLA150 Maskless Aligner, which later served as the mask for the anisotropic etching of a Si wafer using an STS ICP RIE System, to obtain the array of Si microstructures. The geometries and sizes of the structures fabricated for this study are shown in Fig. S4 and Table S1. After removal of the photoresist with oxygen plasma, the Si microstructure array was treated with trichloro(1H,1H,2H,2H-perfluorooctyl) silane to render the structure hydrophobic. Subsequently, the polydimethylsiloxane (PDMS) precursor (mixture of Sylgard 184 base and the crosslinker with the ratio of 10:1 (wt:wt)) was applied on top of the Si wafer, and cured at 70ºC for 2 h. Finally, the PDMS was carefully peeled off from the Si wafer and used as a mold for the synthesis of LCE microstructures.

4.2. Synthesis of LCE microstructures

The obtained LC monomer was well mixed with crosslinker 1,6-hexanediol diacrylate (HDDA; 5% wt/wt based on LC monomer), and photo-initiator 2-hydroxy-2-methylpropiophenone (2% wt/wt based on LC monomer). We applied 20 mg of the reactive mixture into a PDMS mold and covered with a glass substrate. The sample was then placed in a magnetic field generated by the desired assembly of NdFeB-based magnets with surface field of 0.5 T (Fig. S5), heated to 90ºC (isotropic phase), cooled down to 60ºC at a rate of 1ºC/min, and exposed to UV (Dymax Model 2000 Flood UV Curing System, light intensity of ~ 18 mW/cm^2) in a nitrogen atmosphere to initiate polymerization. After 1 h of polymerization, the sample was cooled down to room temperature, and the PDMS mold was carefully peeled off from the LCE microstructures.

4.3. Imaging of deformations of LCE microstructures

Imaging of the LCE deformation was conducted using a Zeiss LSM700 confocal fluorescence microscope equipped with a home-made sample holder to control the temperature of the LCE microstructures. Rhodamine B dye was coated on top of the LCE microstructures for fluorescence microscopy imaging.

4.4. Dimensional changes of exemplary LCE microplates

An LCE microplate with molecular alignment along the Z-axis was made and cut off from the substrate with a razor blade. The unconstrained LCE microplate was placed on the home-made heating stage covered with silicone oil to lower the friction between the LCE microplate and the heating stage. Dimensional changes of the LCE microplate were monitored with the confocal fluorescence microscope, as shown in Fig. S6. Table S2 shows the dimensions of the substrate-attached LCE microplates with different director orientations in their deformed states.

4.5. Influence of surface anchoring on the internal configuration of the LCE microstructures

The LC alignment in the presence of magnetic field is determined by an energetic balance between the free energy contributions arising from a magnetic field and surface anchoring. The free energy induced by the magnetic field can be written as (6):

$$E_{magnetic} = \frac{1}{2} \cdot \frac{\Delta\chi}{\mu_0} B^2 SL$$

in which $\Delta\chi$ is the diamagnetic anisotropy, μ_0 is the free space permeability, B is the strength of the local magnetic field, S is the surface area, and L denotes the thickness of the LC system.

The surface anchoring energy can be expressed as (6):

$$E_{surface} = \frac{1}{2} \cdot WS$$

where W is the surface anchoring strength. Equating these two energetic contributions ($E_{magnetic}$=$E_{surface}$), we define a critical length:

$$L_{crit} = \frac{W\mu_0}{\Delta\chi B^2}.$$

When one dimension of the LCE microstructure is smaller than L_{crit}, the LC will satisfy the surface anchoring condition. By using typical values of numerical parameters in this work (W=$10^{-2}\ mJ \cdot m^{-2}$, $B = 0.5\ T$, $\Delta\chi = 1.0 \times 10^{-7}$, and $\mu_0 = 4\pi \times 10^{-7}\ kg \cdot m \cdot S^{-2} \cdot A^{-2}$) (7,8), we calculated L_{crit} to be ~ 5 μm. Fig. S7 demonstrates that an array of 5 μm-wide microplates undergo non-uniform deformations, which do not correspond to the magnetic field-encoded director orientation (as the magnetic field is along the Z-axis of the microplates during polymerization). For the LCEs thicker than L_{crit}, the mesogens in the bulk will follow the direction of the external magnetic field. Therefore, in this work we chose microstructures with the dimensions in the range of 25-250 μm, for which the internal molecular alignment is mainly controlled by the external magnetic field. However, L_{crit} still limits the patterning resolution of the molecular alignment.

4.6. Reversibility of the LCE microplate deformation

Reversibility of the deformation was studied using an LCE microplate with the director oriented in the X-Z plane undergoing out-of-plane tilting. Measurements of 20 actuating cycles immediately after synthesis and 180 more cycles nine months later demonstrate long-term reversibility with negligible deterioration (Fig. S8).

4.7. Comparison between the tilting angles of differently oriented microplates

To study the effect of the bending stiffness on the tilting angle of the deformation, we fabricated a microstructure array comprised of microplates facing different directions (along the X-axis, along the Y-axis, and at ±45° to the X- and Y-axes), but having the same global alignment of their mesogens within Y-Z plane, as shown in Fig. 2*A* in the main text. The LC configuration was controlled by the magnetic field to be close to 45° with respect to the Z-axis. Based on the dimension of the microplates (250 μm-in-length, 50 μm-in-width and 200 μm-in-height), the bending stiffness of the in-plane tilting with the director in the Y-Z plane ($\sim Ea^3b$, where E denotes the elastic modulus of the material, a and b are the lengths of the long and short axes of the microstructure in the X-Y plane, respectively) is 24 times higher than that of the out-of-plane tilting with the director in the X-Z plane ($\sim Eab^3$). However, the whole array showed identical tilting angles (~ 55°) according to the active deformation mechanism of LCEs.

4.8. Control over the twisting of microplates

Instead of doping chiral molecules as in previous studies (9), we can introduce and control the handedness of LCE microplate deformation by tuning the LC director with respect to the long axis of the microplate. When the director is in the regions marked by 'R' (or 'L') as shown in Fig. 2*C* in the main text, the microplate adopts a right-hand (or left-hand) twisting deformation during the N-I phase transition. Importantly, the experimentally observed twisting angle is significantly larger than the one predicted by modeling, when the mesogen alignment is 45° relative to the X-axis in the X-Y plane. We attribute this effect to the contribution from the LCE film at the base of the molded structures (see Fig. S5b), which is likely moving together with the structures, thus amplifying the overall deformation.

Indeed, including the LCE base in the computer simulations results in an increase in the twist angle that increases with the thickness of the film, confirming the hypothesized role of the base layer (Fig. S9). In contrast to the plate, the LCE thin film in the simulations is assumed to have a director oriented by surface anchoring within the region (smaller than L_{crit}) next to the glass substrate rather than along the magnetic field (as discussed in Section 4.5). The nodes at the bottom layer of this base are held fixed (representing their adhesion to the glass slide) while the upper layers are free to move. When increasing the thickness of the base, both the portion of mesogens aligned by the magnetic field and the flexibility of the base increase, thereby increasing the twist.

4.9. Deformation of the LCE honeycomb structures

As described in Fig. 3 of the main text, the deformation behavior of the geometrically identical honeycomb-like cellular structures upon heating can be controlled by tuning the internal molecular configuration of LCE in magnetic field during polymerization. When

the internal molecular alignment was along the Z-axis, the structure showed a highly regular buckling pattern upon N-I phase transition, resulting from a uniaxial contraction along the director and a corresponding expansion in the X-Y plane (10). When the director was in the X-Z plane and 45^{o} with respect to the Z-axis, the structure showed a tilting/shearing deformation. More interestingly, when the director was along the Y-axis, the initial hexagonal structure transformed into a rectangular brick pattern due to a globally uniaxial contraction along the director.

5. Hierarchical deformation of the LCE microstructure array

5.1. Assembly of LCE microstructure arrays

The magnetic field with two-fold symmetry was achieved by assembling three block magnets (with the dimensions of 2.5 cm x 1.25 cm x 1.25 cm) side by side; the 'T'-shaped magnetic field was generated by having two block magnets aligned in a "head to side" manner; the magnetic field with the four-fold symmetry was produced using five disk magnets (with diameter of 2.5 cm, and thickness of 1 cm), all of which are shown in the schematics in Fig. S10, where only the top half of the magnets is shown. All magnets with desired geometries were constructed in COMSOL Multiphysics using the Magnetic Field Module. The magnets were assigned a surface magnetic field of 0.5 T, from which the resulting magnetic field patterns were calculated. The results are shown in Fig. S10. Fig. S10a shows the 2D projection of the magnetic field on the X-Z plane in the middle of the magnets, while both Fig. S10b and c illustrate the 2D projection on the X-Y plane right above the magnet.

Fluorescence confocal micrographs of LCE microstructure arrays polymerized in various complex magnetic fields are shown in Fig. S10. The micrographs correspond to the results quantified in Fig. 4*A-C* of the main text. Each of the white arrows in Fig. S10 denotes the vector connecting the centers of the top surface of an LCE microplate in its undeformed and deformed states at the corresponding position. As a result, the direction of arrows shows the azimuthal tilting angle and the length quantifies the polar tilting angle.

5.2. Controlled adhesive system

A microstructured epoxy sample was prepared by UV-initiated polymerization of an epoxy precursor (NOA61, Norland Products) sandwiched between a PDMS mold and a cover slip glass substrate. Two circular cover slips taped to the backside of the epoxy microstructural substrate were used as cargo (total weight of the load: 560 mg). An LCE structural array of ~ 85 microplates distributed in an area of 15 mm x 10 mm was taped to a heating pad and placed vertically. The epoxy microstructure array was stacked on the LCE counterpart prior to studying the thermally-induced release of the epoxy cargo.

5.3. LCE microstructure arrays for information encryption

We used step-wise polymerization to encode area-specific molecular configurations into the LCE array. The first step of UV-induced polymerization was carried out under an 'H'-patterned photomask in the absence of a magnetic field at 100^{o}C for 10 min in Dymax Model 2000 Flood UV Curing System. Subsequently, we removed the

photomask, slowly cooled the system down (1ºC/min) to 60ºC, and conducted the second polymerization in the presence of the magnetic field.

6. Light-responsive LCE microstructures

6.1. Synthesis of light-responsive LCE micropillars

To synthesize photo-responsive LCE micropillars, the azobenzene derivative 4,4'-bis(6-acryloyloxyhexyloxy) azobenzene (7.5% wt/wt based on LC monomer) was added into the reactive mixture described in Section 4.2; the photo-initiator was changed to bis(2,4,6-trimethylbenzoyl)-phenylphosphineoxide (2% wt/wt based on LC monomer) in order to initiate the polymerization with longer wavelengths. The sample was placed in a magnetic field, heated to 75ºC, cooled down to 45ºC at a rate of 1ºC/min, and exposed to UV for 1 h. The UV/Vis absorption spectrum of the azobenzene derivative showed a strong peak at ~ 360 nm, corresponding to its *trans* to *cis* conversion (Fig. S11). To keep the azobenzene moiety in its *trans* state, the system was covered by an optical filter that blocks the light with wavelength shorter than 400 nm during the 1 h polymerization under nitrogen atmosphere. Light-responsive micropillars were 25 μm-in-diameter and 75 μm-in-height.

6.2. Phase behavior of the LC monomer mixture and the polymeric network

After doping azobenzene derivative, the reactive mixture showed a nematic phase for temperatures between 20ºC and 70ºC (Fig. S12a,b). The polymerized photo-responsive LCE showed a nematic-isotropic phase transition at ~90ºC (Fig. S12c,d).

6.3. Light-responsive deformations of the LCE micropillars

The light-responsive deformation of LCE micropillars containing azobenzene derivatives was characterized by using confocal fluorescence microscopy. During the characterization, a handheld UV light (HeroFire UV365NM) was placed 5 cm from the sample and 45º with respect to the Z-axis (3.5 mW/cm^2), and the temperature of the sample was kept at 70ºC.

To further characterize the bending angle of LCE micropillars with respect to the UV illumination angle, we mounted the sample onto a homemade heater attached to a temperature controller (J-Kem Scientific, Model APOLLO) to maintain the temperature at 70ºC. The heater was then placed vertically under an upright white light optical microscope (Leica DMRX) to enable observation of the side-view of the micropillars. The UV lamp was placed at 5 cm from the sample.

6.4. Dependence of the bending angle on the illumination direction

Bending of micropillars in response to the direction of UV illumination was characterized by using the home-made experimental setup illustrated in Fig. S13a. The UV light was placed 3.5 cm from the sample, with its rotational axis coinciding with the imaged region of the sample. The sample was initially illuminated for 150 s to reach equilibrium. The illumination angle was then changed in steps of 5º followed by 90 s equilibration time before capturing each image. As shown in Fig. S13b, we observed the tip bending angle to change from 0º to 20º as the UV illumination angle increased from 0º to 30º. We did

not test UV illumination angles beyond 30°, as pillar-pillar shadowing prevents full exposure to UV light for all micropillars.

6.5. Self-regulated antenna

The UV-responsive LCE micropillar array was coated with 10 nm of titanium and 100 nm of silver using directional e-beam evaporation (Denton) to prevent metal coating on the sidewall of micropillars. The thin silver layer served as a mirror, so that the tips of micropillars appeared bright when they directly faced the objective lens and dark when tilted (due to sample mounting; Fig. S14) or bent away (by UV actuation; Fig. 6*C* of the main text) from the lens under the upright white light optical microscope.

The sample was first mounted on the upright optical microscope with a tilting angle of β (20 degrees for the optical image in Fig. S14). In the absence of UV illumination, the imaging light was reflected at an angle of 2β with respect to the incoming light and thus was not captured by the objective lens (for $\beta \neq 0$), so that the image appeared dark (Fig. S14, left inset). However, UV exposure at the appropriate angle (30 degrees in experiments), as determined from Fig. S13b, actuated the LCE pillars such that the micropillar tips became normal to the incident light and the light collected by the objective increased significantly (Fig. S14, right inset).

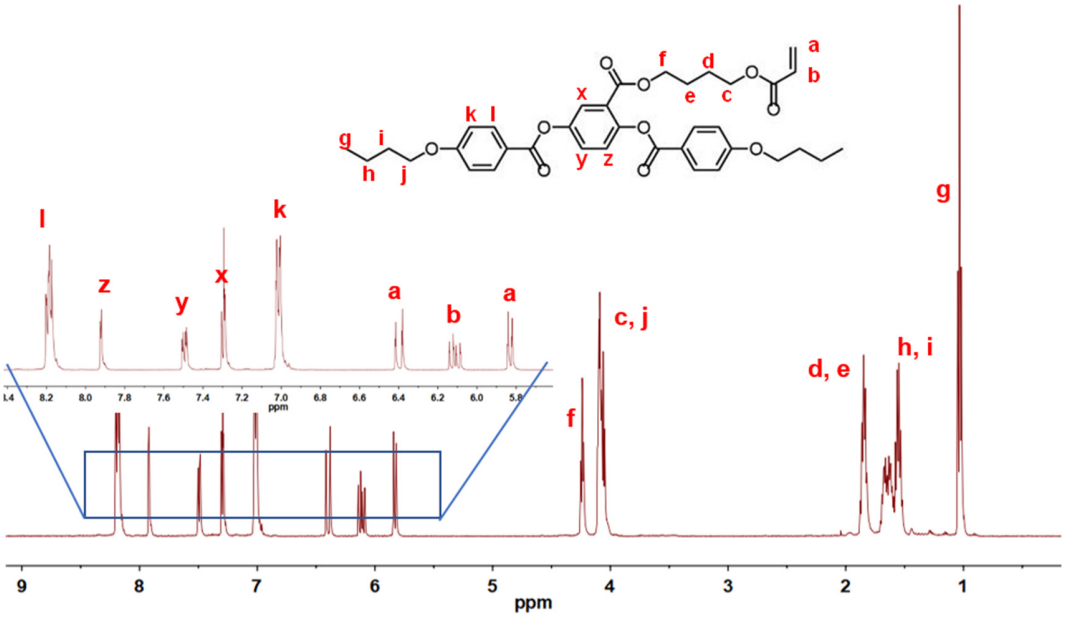

Fig. S1. ^{1}H spectrum of LC monomer 4″-acryloyloxybutyl 2,5-di(4′-butyloxybenzoyloxy) benzoate.

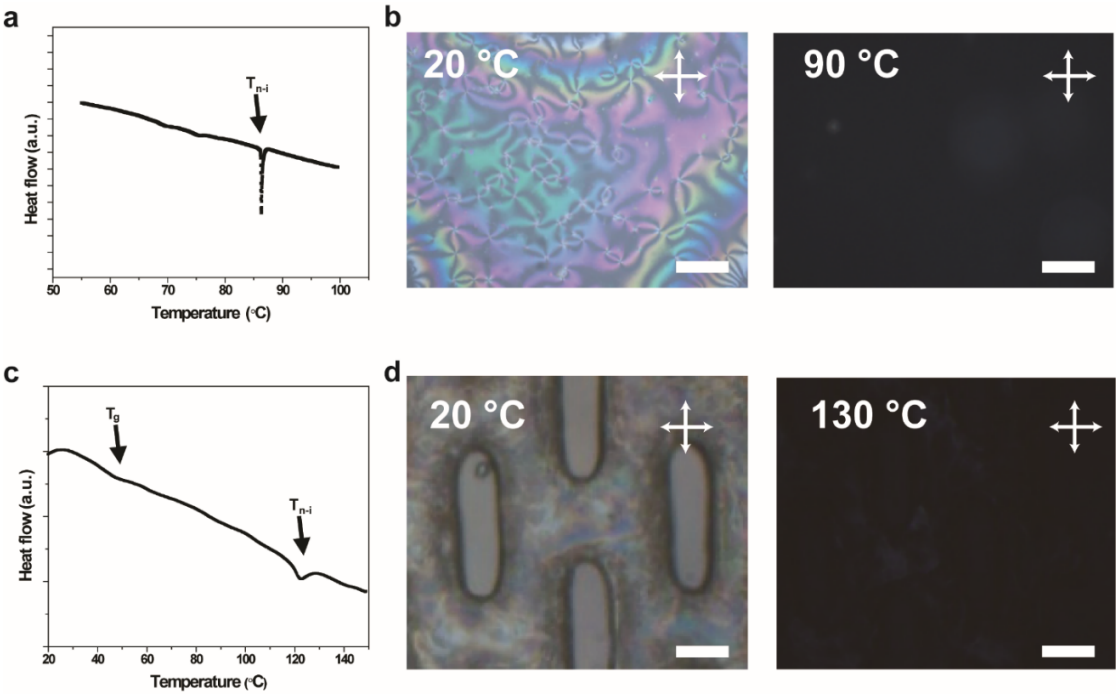

Fig. S2. (a,c) Phase diagrams and (b,d) polarized light micrographs of (a,b) the thermal-responsive LC monomer mixture, and (c,d) the corresponding polymerized LCE. The heating rate in the differential scanning calorimetry (DSC) measurement is 10°C/min. Scale bars, 100 μm.

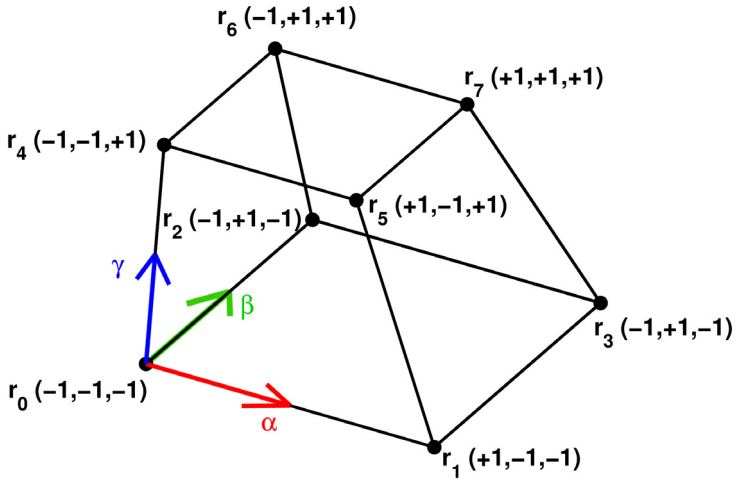

Fig. S3. Diagram of a finite element. Vertices are indexed as shown within each element, with coordinates (α, β, γ) for each point given in parentheses. The material-frame axes initially coincide with the axes in the lab frame. As the material deforms, the lab frame coordinates of the nodes will change, but their material frame coordinates will remain fixed.

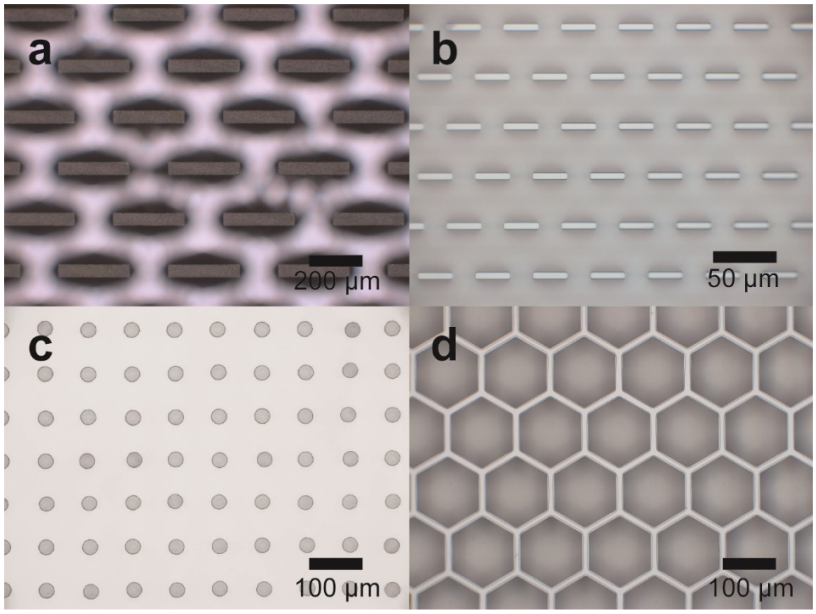

Fig. S4. Optical micrographs of Si microstructures corresponding to Table S1.

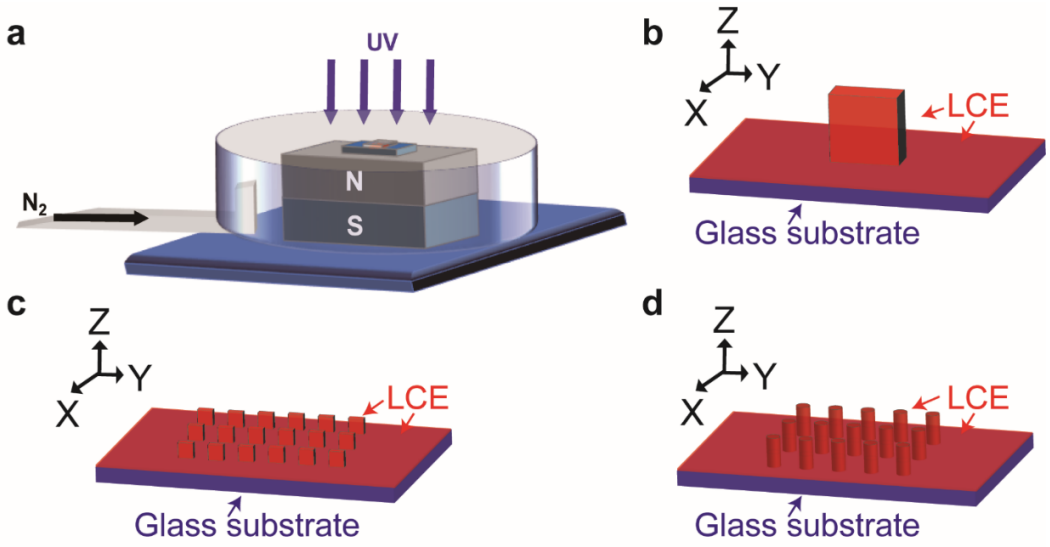

Fig. S5. Synthesis of LCE microstructures aligned in a magnetic field. (a) Exemplary setup for the synthesis of the LCE microstructures with the LC director oriented in the Z-axis direction. (b-d), Schematics of (b) a fabricated isolated LCE microplate, (c) an array of microplates, and (d) an array of micropillars. Note that there is a thin layer of LCE in between microstructures and the glass substrate.

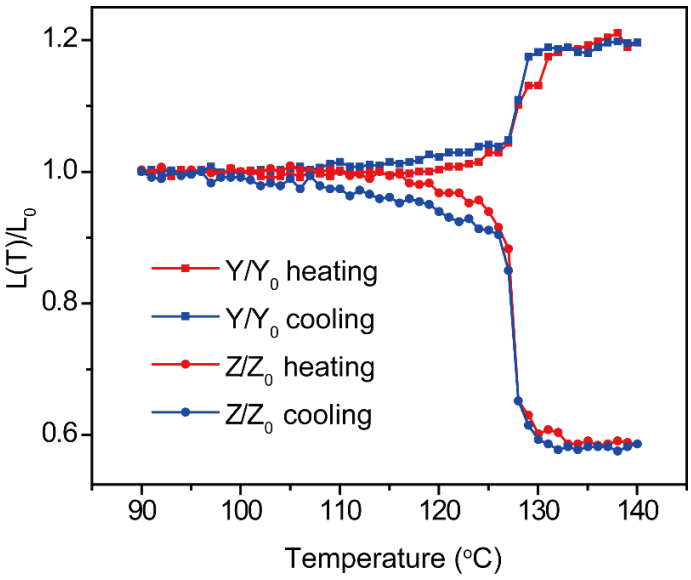

Fig. S6. Dimensional changes of the LCE microplates as a function of temperature. L(T) and L_0 represent the dimensions of the microstructure at temperature T and room temperature, respectively. Y and Z measure the length of LCE microplates perpendicular and along the molecular alignment, respectively.

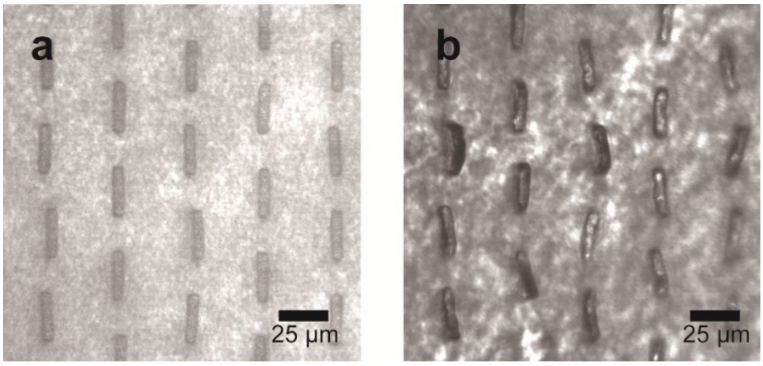

Fig. S7. The deformation of LCE microplates aligned by the surface anchoring with its smallest dimension smaller than L_{crit}.

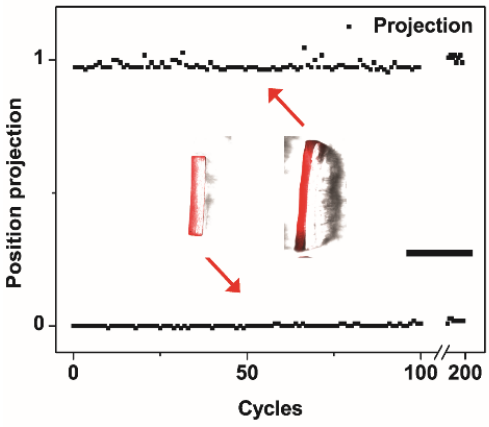

Fig. S8. Reversibility of the LCE microplate deformation. The Y-axis represents the displacement of the tip, where 0 indicates no displacement relative to the initial position, and 1 corresponds to the displacement of the microplate's average position above T_{N-I} in the first 20 cycles. Scale bar, 200 μm.

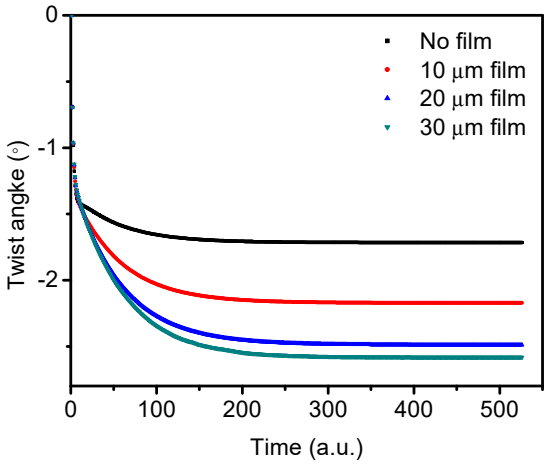

Fig. S9. Finite element simulations of the twist angles of LCE microplates with different thickness of LCE base layers.

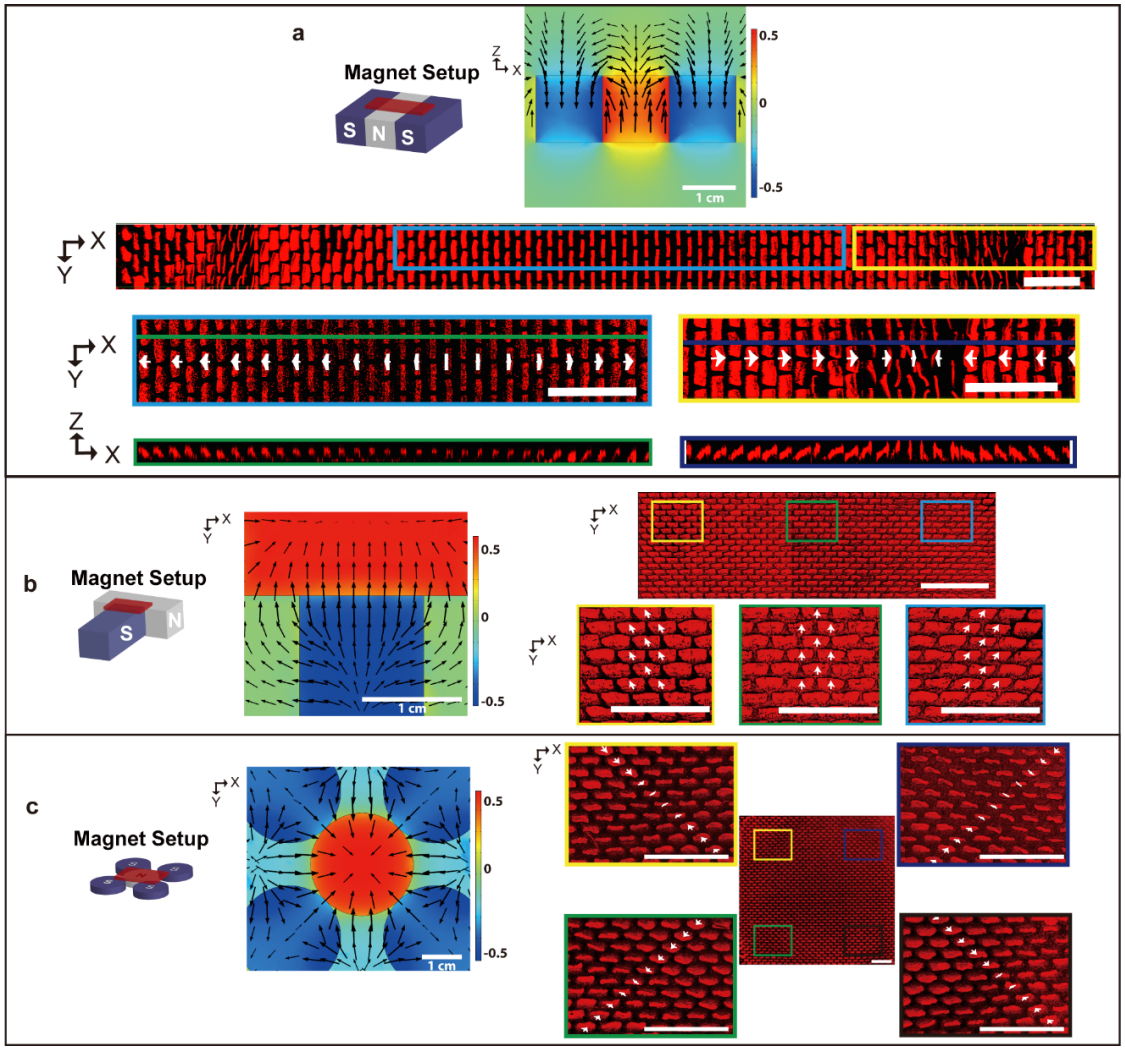

Fig. S10. Schematics and COMSOL simulations of the magnetic field and confocal images of the microstructural assembly of LCE microplates with (a) a two-fold, (b) "T"-shape, or (c) four-fold symmetry. Scale bars: 1mm.

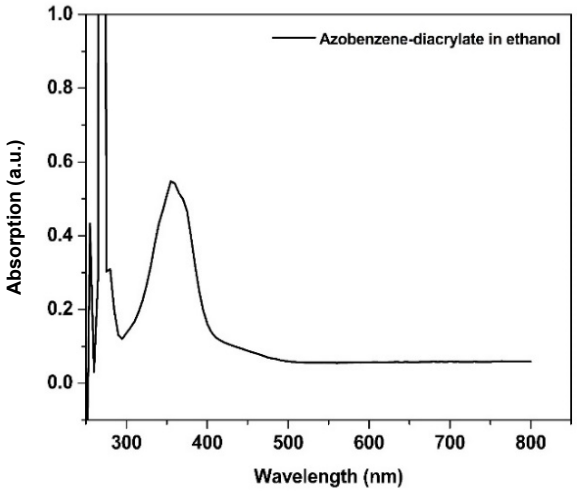

Fig. S11. The UV/Vis spectrum of azobenzene crosslinker 4,4'-bis(6-acryloyloxyhexyloxy) azobenzene in ethanol solution.

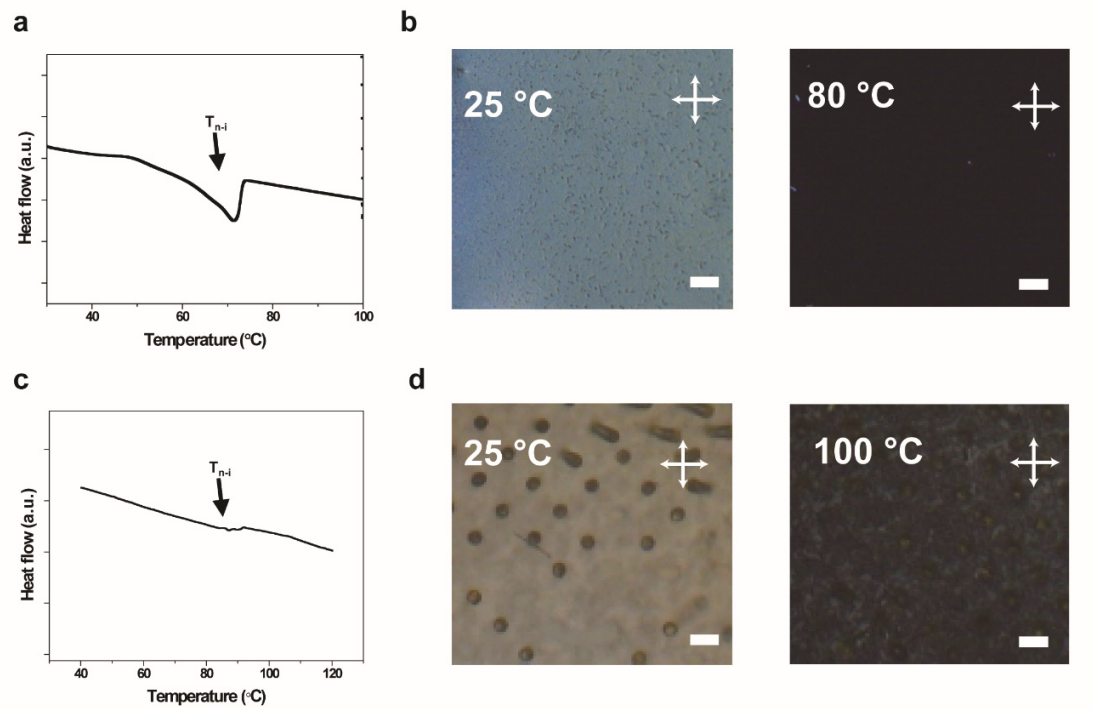

Fig. S12. (a,c) Phase diagrams and (b,d) polarized light micrographs of (a,b) the light-responsive LC monomer mixture, and (c,d) the corresponding polymerized LCE. The heating rate in the DSC measurement is 10ºC/min. Scale bars, 100 μm.

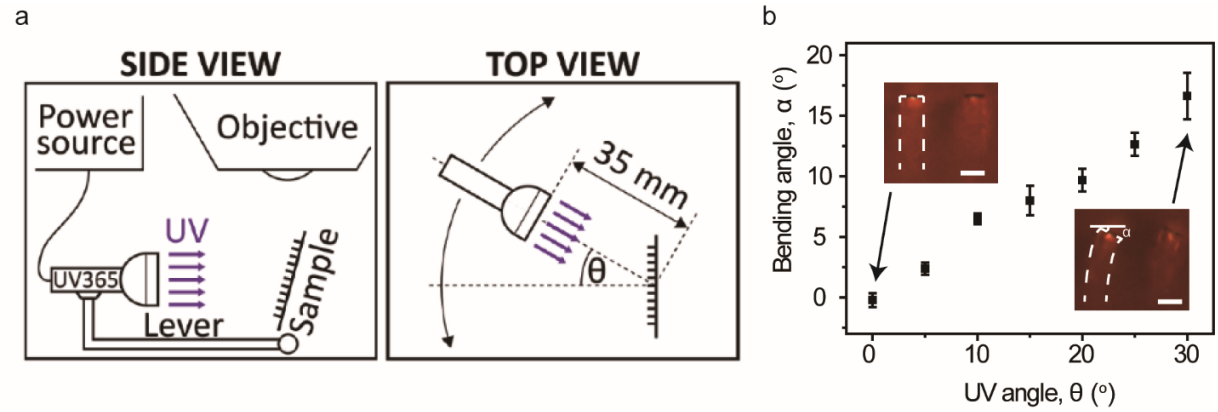

Fig. S13. Influence of UV illumination direction on the bending angle of micropillars. (a) Schematic illustration of the experimental setup for the characterization of the bending angles of photo-responsive micropillars. (b) The bending angle of the micropillars as a function of the UV illumination angle. Insets show representative optical micrographs of micropillars with and without UV exposure. Scale bars, 25 μm.

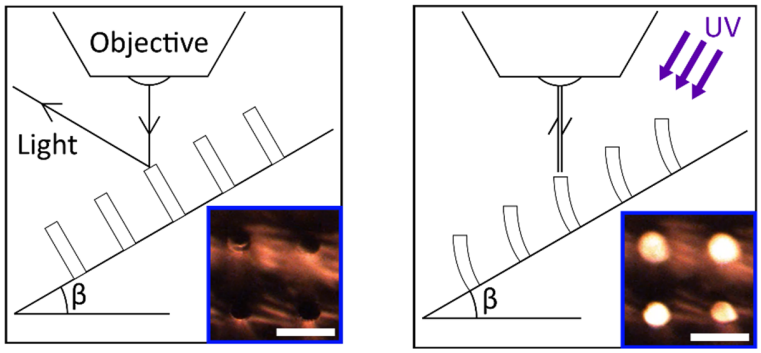

Fig. S14. Schematic illustration of self-regulated antenna. Insets show the optical reflection of the LCE tips. Scale bars, 50 μm.

Table S1. Dimensions of different LCE microstructures fabricated.

3D microstructures	Dimensions
a. Microplates	250 μm (length) * 50 μm (width) * 200 μm (height)
b. Microplates	25 μm (length) * 5 μm (width) * 20 μm (height)
c. Micropillars	25 μm (diameter) * 75 μm (height)
d. Honeycomb microstructures	60 μm (inner length), 15 μm (wall thickness), and 100 μm (height)

Table S2. Dimensional changes of LCE microplates with different director orientations.

Director orientation	Dimensions
Z-axis (Fig. 1 (ii))	300 μm (length) * 65 μm (width) * 145 μm (height)
Y-axis (Fig. 1 (iii))	130 μm (length) * 65 μm (width) * 220 μm (height)
X-Z plane (Fig. 1 (iv))	335 μm (length) * 30 μm (width) * 120 μm (height)
Y-Z plane (Fig. 1 (v))	220 μm (length) * 58 μm (width) * 140 μm (height)
X-Y plane (Fig. 1(vi))	220 μm (length) * 50 μm (width) * 196 μm (height)

Captions for movies S1 to S7

Movie S1.

Top left, the top view of uniaxial contraction of a thermal-responsive LCE microplate along its long axis. The LC mesogens within the microplate are aligned along the Y-axis. Top right, the top view of out-of-plane tilting of a thermal-responsive LCE microplate. The LC mesogens within the microplate are aligned in the X-Z plane. Bottom left, the top view of in-plane tilting of a thermal-responsive LCE microplate. The LC mesogens within the microplate are aligned in the Y-Z plane. Bottom right, the top view of twisting of a thermal-responsive LCE microplate. The LC mesogens within the microplate are aligned in the X-Y plane.

Movie S2.

Shape-memory effect of LCE microstructures. Once the micropillars were deformed by an arbitrary external force, we recovered their original state by heating the sample above the glass transition temperature (T_g).

Movie S3.

Left, the top view of buckling of a thermal-responsive LCE honeycomb structure. The LC mesogens within the structure are aligned along the Z-axis. Middle, the top view of tilting of a thermal-responsive LCE honeycomb structure. The LC mesogens within the microplate are aligned in the X-Z plane. Right, the top view of the lattice transformation of a thermal-responsive LCE honeycomb structure. The LC mesogens within the microplate are aligned along the Y-axis.

Movie S4.

Controlled adhesive system based on an LCE microstructural surface. When the temperature reached 130ºC (above T_{N-I}), the LCE microstructures underwent pre-designed downward tilting, resulting in unloading of the epoxy microstructural cargo, which remained on the LCE surface below T_{N-I}.

Movie S5.

Top view of light-responsive self-adaptive deformation of LCE micropillars. The UV-responsive micropillars showed self-regulated bending towards the light source.

Movie S6.

Side view of light-responsive self-adaptive deformation of LCE micropillars. The tips of the UV-responsive micropillars changed their bending angles relative to the substrate in a self-regulated mode.

Movie S7.

Self-regulated antenna. The microstructure array was fabricated as described in Section 6.5. The sample was pre-tilted and showed weak reflection under the upright optical microscope. By adjusting the direction of the UV source, the micropillars can show strong light reflection, giving rise to a bright appearance at their tips.

References

1. Thomsen DL, Keller P, Naciri J, Pink R, Jeon H, Shenoy D, Ratna BR (2001) Liquid crystal elastomers with mechanical properties of a muscle. *Macromolecules* 34:5868-5875.
2. Horgan CO (2015) The remarkable Gent constitutive model for hyperelastic materials. *Int J Non Linear Mech* 68:9-16.
3. Horgan CO, Saccomandi G (2002) A molecular-statistical basis for the Gent constitutive model of rubber elasticity. *J Elast* 68:167-176.
4. Mbanga BL, Ye F, Selinger JV, Selinger RLB (2010) Modeling elastic instabilities in nematic elastomers. *Phys Rev E* 82:051701.
5. Terentjev EM, Warner M (2003) Liquid Crystal Elastomers (Oxford Univ Press, Oxford).
6. Miller DS, Wang X, Abbott NL (2014) Design of functional materials based on liquid crystalline droplets. *Chem Mater* 26:496-506.
7. de Gennes PG (1974) The Physics of Liquid Crystals (Oxford Univ Press, Oxford).
8. Xia Y, Lee E, Hu H, Gharbi MA, Beller DA, Flesichmann E, Kamien RD, Zentel R, Yang S (2016) Better actuation through chemistry: using surface coatings to create uniform director fields in nematic liquid crystal elastomers. *ACS Appl Mater Interfaces* 8:12466-12472.
9. Sawa Y, Ye F, Urayama K, Takigawa T, Gimenez-Pinto V, Selinger RLB, Selinger JV (2011) Shape selection of twist-nematic-elastomer ribbons. *Proc Natl Acad Soc USA* 108:6364-6368.
10. Kang SH, Shan S, Noorduin WL, Khan M, Aizenberg J, Bertoldi K (2013) Buckling-induced reversible symmetry breaking and amplification of chirality using supported cellular structures. *Adv Mater* 25:3380-3385.